ACS APPLIED MATERIALS & INTERFACES

Research Article

www.acsami.org

# High-Performance Organic Complementary Inverters Using Monolayer Graphene Electrodes

Yong Jin Jeong, Jaeyoung Jang, Sooji Nam, Kyunghun Kim, Lae Ho Kim, Seonuk Park, Tae Kyu An, and Chan Eon Park*

Polymer Research Institute, Department of Chemical Engineering, Pohang University of Science and Technology, Pohang 790-784, Korea

Supporting Information

**ABSTRACT:** Chemical vapor deposition-grown graphene has been an attractive electrode material for organic electronic devices, such as organic field-effect transistors (OFETs), because it is highly conductive and provides good oxidation and thermal stability properties. However, it still remains a challenge to demonstrate organic complementary circuits using graphene electrodes because of the relatively poor performance of *n*-type OFETs. Here, we report the development of high-performance organic complementary inverters using graphene as source/drain electrodes and N, N′-ditridecyl-3,4,9,10-perylenetetracarboxylic diimide (PTCDI-C13) and pentacene as *n*- and *p*-type organic semiconductors, respectively. Graphene electrodes were *n*-doped via the formation of $NH_2$-terminated self-assembled monolayers that lowered the work function and the electron injection barrier between the graphene and PTCDI-C13. Thermal annealing improved the molecular packing among PTCDI-C13 groups on the graphene surface, thereby increasing the crystallinity and grain size. The thermally annealed PTCDI-C13 OFETs prepared using *n*-doped graphene electrodes exhibited a good field-effect mobility of up to 0.43 $cm^2/(V\ s)$, which was comparable to the values obtained from other *p*-type pentacene OFETs. By integrating *p*- and *n*-type OFETs, we successfully fabricated organic complementary inverters that exhibited highly symmetric operation with an excellent voltage gain of up to 124 and good noise margin.

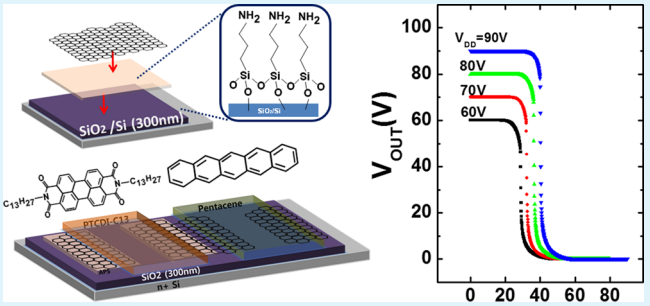


**KEYWORDS:** *graphene, chemical vapor deposition, n-type organic semiconductors, organic complementary inverters, work function, thermal annealing*

## INTRODUCTION

Organic field-effect transistors (OFETs) have received great interest as a key element for all-organic electronics applications aimed at realizing low-cost, lightweight, and flexible devices because of the advantages of low-temperature processing.[1−3] OFETs may be integrated into such devices preferably using complementary logic gates consisting of *p*- and *n*-type transistors rather than unipolar logic gates because complementary logic gates consume low power levels, provide good noise margins, and display robust operation.[4−6] Balancing the performances of *p*- and *n*-type OFETs is essential for achieving high-performance organic complementary inverters; however, *n*-type OFETs generally display a lower performance and stability compared to *p*-type devices.[7] Significant efforts have been applied toward enhancing the performances of *n*-type OFETs through, for example, the rational design of *n*-type organic semiconductors in an effort to achieve a high oxidation stability and electrical performance.[8−11] Interface engineering between the semiconductor and the dielectric has also been attempted using hydrophobic self-assembled monolayers (SAMs) or polymers.[7,12−15] These approaches have improved device performance and stability. As the field has progressed, the need for appropriate electrode materials for use in *n*-type OFETs has grown urgent. Low work function metals (e.g., aluminum and calcium), which are used for efficient carrier injection, are generally poorly stable to oxidation, which hinders device applications.[16−18] For example, these metal electrodes are unsuitable for OFETs prepared using the bottom-contact geometry, which can be a desirable device structure for certain commercial OFET applications. Because the metal electrodes can be readily oxidized, thin oxide layers form atop the electrodes and significantly impede charge injection into the organic semiconductor layers.[18,19]

Recently, graphene films synthesized in large scale by chemical vapor deposition (CVD) methods have been considered as attractive source/drain (S/D) electrodes materials for OFETs because of their high electrical conductivity and good oxidation/thermal stabilities.[20−24] The thinness (< 3−4 Å) and two-dimensionally flat structure of the monolayer graphene films facilitated the coverage and self-

Received: January 28, 2014
Accepted: April 14, 2014
Published: April 14, 2014

   dx.doi.org/10.1021/am500618g | ACS Appl. Mater. Interfaces 2014, 6, 6816−6824

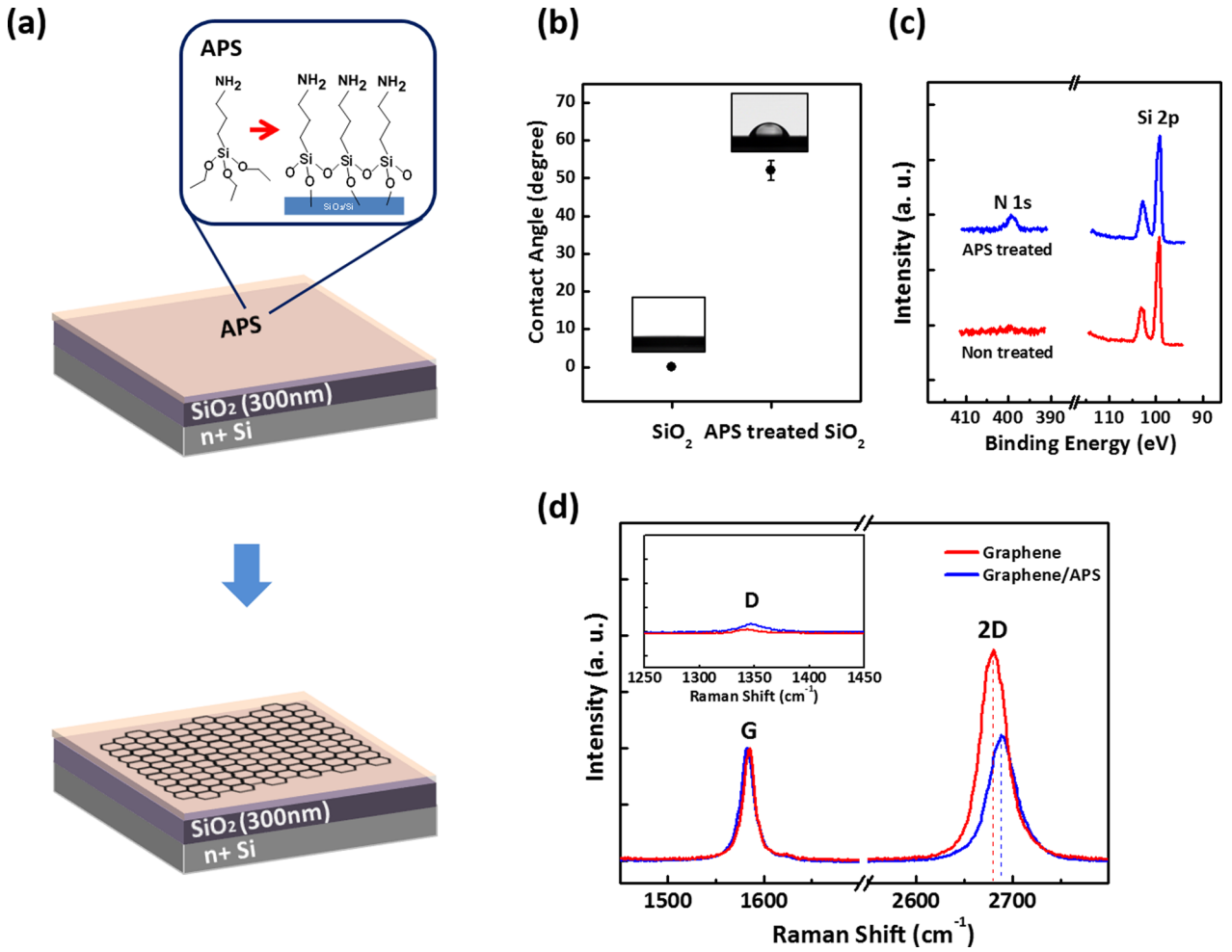


**Figure 1.** (a) Schematic illustration of the experimental procedure and sample structure used in this study. Inset: chemical structures of 3-aminopropyltriethoxysilane (APS). (b) Comparison of the water contact angles $\theta_{water}$ measured on the pristine and APS-modified $SiO_2$ substrates. The inset shows the captured optical images of seeded water drops on each substrate. (c) XPS profiles of pristine (red) and APS-modified $SiO_2$/Si (blue) substrates. (d) Raman spectra of graphene on pristine $SiO_2$/Si(red) and APS-doped graphene on APS-modified $SiO_2$/Si substrates (blue).

organization of the overlying organic semiconductors in bottom-contact OFETs.[25−27] In addition, it has been reported that the work function of a graphene film may be tuned via chemical doping (e.g., by introducing functionalized SAMs beneath the graphene).[28−30] The use of n-doped graphene films as S/D electrodes in *n*-type OFETs has recently been demonstrated. The performances of the resulting OFETs, however, were not satisfactory (mobility ≤0.1 $cm^2/(V\ s)$),[30] possibly because the molecular ordering and grain growth of the organic semiconductor material was not optimized on graphene so that the interface between the graphene and OFET channel impeded operation. The benefits of graphene S/D electrodes may only be realized by optimizing the crystallinity and molecular packing of organic semiconductors toward enhancing device performance.

Here, we studied the effects of thermal annealing on the crystallinity and morphology of *n*-type organic semiconductor layers deposited on graphene S/D electrodes. We additionally characterized the performances of the resulting OFETs. *N,N′*-Ditridecyl-3,4,9,10-perylenetetracarboxylic diimide (PTCDI-C13) was used as the semiconductor material. PTCDI-C13 is an *n*-type organic semiconductor commonly used in OFETs because it is highly crystalline, with large grain sizes after thermal treatment because of its strong self-organization properties.[7,31] Efficient electron injection was achieved by reducing the work function of the graphene electrodes via chemical doping introduced by forming an electron-donating $NH_2$-terminated SAM.[30,32] The thermally annealed PTCDI-C13 thin films formed highly crystalline domains with large grains on the graphene electrodes, where PTCDI-C13 molecules were favorably stacked for lateral charge transport. The OFETs prepared with graphene S/D electrodes exhibited good performances, with an average mobility of 0.40 $cm^2/(V\ s)$, comparable to *p*-type pentacene OFETs. The balance between the individual *n*- and *p*-type OFETs enabled the preparation of high-performance organic complementary inverters based on graphene electrodes with an excellent voltage gain of up to 124 and a good noise margin.

## EXPERIMENTAL METHODS

The $NH_2$-terminated SAMs were prepared by treating 300 nm thick $SiO_2$/Si gate substrates with 3-aminopropyltriethoxysilane (APS) $(NH_2(CH_2)_3Si(OC_2H_5)_3$, 99%, Aldrich Co.), as shown in Figure 1a. Prior to APS treatment, the substrate was cleaned in a piranha solution, followed by multiple rinses with DI water. The hydrophilicity of the surface was then increased by applying UV-ozone treatment for 20 min. The substrates were dipped in a 0.3 mM APS solution in toluene for a few seconds and subsequently baked at 120°C for 20 min, followed by sonication in toluene for 15 min.[33]

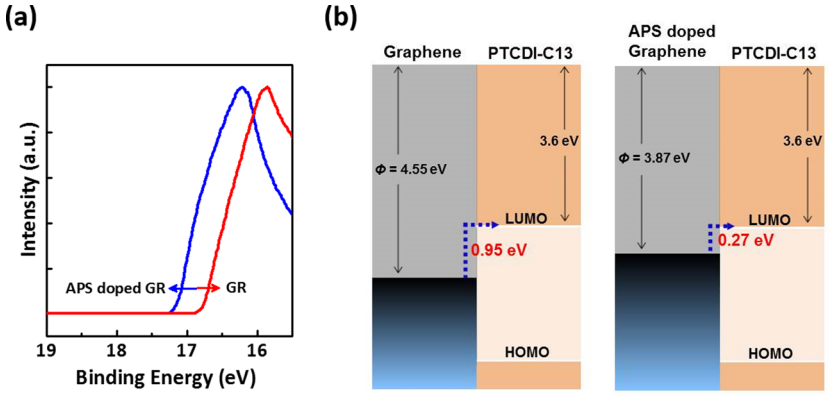


**Figure 2.** (a) Comparative UPS spectra showing the secondary cutoff regions of pristine and n-doped graphene films. (b) Schematic energy diagrams of the interface between the pristine or n-doped graphene electrodes and the overlying PTCDI-C13 films, including the work function of the graphene films and the injection barriers. Electron injection barriers between the pristine or n-doped graphene films and the PTCDI-C13 films were calculated from the UPS data and the reported energy levels of the PTCDI-C13 films.[30,38]

Monolayer graphene was synthesized on a 25 $\mu$m thick copper foil using CVD methods under low-pressure conditions, as described previously.[22] Solutions of poly(methyl methacrylate) (PMMA) were spin-coated onto the graphene film to form a supporting layer during graphene transfer. The copper foil was etched away using 0.1 M ammonium peroxydisulfate ($(NH_2)_4S_2O_8$, 98%, Kanto Co.). The graphene film supported by the PMMA layer was transferred onto the APS-modified substrate and patterned into S/D electrodes using photolithography, as described previously.[34] The optical images of patterned graphene electrodes of OFETs are shown in Figure S1a in the Supporting Information. The OFET channel length ($L$) and width ($W$) were 100 and 1000 $\mu$m, respectively. $n$-Type OFETs were fabricated by depositing a 50 nm thick PTCDI-C13 (Aldrich Co.) active layer (at a rate of 0.2 Å/s) onto the substrates supporting graphene S/D electrodes using an organic molecular beam deposition system. The PTCDI-C13 thin films were thermally annealed at 130 °C for 1 h and then slowly cooled to room temperature in a vacuum chamber.

For the fabrication of organic complementary inverters, we patterned the APS SAM on the substrate by exposing UV-ozone through a shadow mask prior to graphene transfer because $p$-type OFETs did not require $n$-doped graphene electrodes (see Figure S2 in the Supporting Information for the detailed fabrication procedure). After patterning the APS SAM, graphene was transferred onto the substrate and patterned to form S/D electrodes for the $n$- and $p$-type OFETs (see Figure S1b in the Supporting Information for the optical image of patterned graphene electrodes of inverter). PTCDI-C13 or pentacene (Aldrich Co.) layers, 50 nm thick, were deposited onto the areas containing APS-doped graphene electrodes or the pristine graphene electrodes (i.e., the APS-free areas), respectively. Prior to pentacene deposition, the PTCDI-C13 thin films were thermally annealed, as described above, to improve the device performance. The inverter consisted of the load transistor (PTCDI-C13 $n$-type OFET) and the drive transistor (pentacene $p$-type OFET) with dimensions of $W/L$= 1600 $\mu$m/150 $\mu$m. All fabrication steps were performed under ambient air (RH: 40% ± 10%).

All electrical measurements were performed using Keithley 4200 SCS in a $N_2$-rich glove box. The morphologies of the PTCDI-C13 films were investigated using atomic force microscopy (AFM, Multimode AFM, Digital Instruments), and x-ray diffraction (XRD) analyses was conducted using a synchrotron X-ray beam source at the 5A beamline in Pohang Accelerator Laboratory (PAL). The work function of the graphene electrodes was characterized using ultraviolet photoelectron spectroscopy (UPS) at the 4D beamline in PAL. The APS SAM was studied using X-ray photoelectron spectroscopy (XPS) (Quantum 2000) and contact angle methods (SEO300A).

## RESULTS AND DISCUSSION

The water contact angles ($\theta_{water}$) on the pristine or APS-modified $SiO_2$/Si substrates were measured to confirm whether the substrates were effectively modified with APS. As shown in Figure 1b, the values of $\theta_{water}$ on the pristine $SiO_2$/Si substrates were about ~0°, whereas those on APS-modified $SiO_2$/Si substrates were ~52 ± 3° in good agreement with the reported values for the APS-modified $SiO_2$/Si substrates.[35,36] For further confirmation, chemical information from the N 1s and Si 2p core level spectra was obtained using XPS analyses of the surfaces of pristine and APS-modified $SiO_2$/Si substrates (Figure 1c). The N 1s peak was clearly observed in the APS-modified samples, whereas no N 1s peak was observed in the pristine samples. Although Si 2p peaks were observed in both samples, the peak did not arise from the APS layer, but rather from the $SiO_2$/Si substrates. These results suggested that the surface of $SiO_2$/Si substrate was successfully modified with APS. The effects of the underlying APS SAM on the properties of graphene were examined by measuring the Raman spectra of the graphene films mounted on pristine and APS-modified substrates. From the Raman spectra, as shown in Figure 1d, the graphene film is mostly monolayer,[22,23,25] and the 2D peak position of the graphene film shifted from 2675 $cm^{-1}$ on pristine $SiO_2$/Si to 2687 $cm^{-1}$ on APS-modified $SiO_2$/Si. In addition, the ratio of the 2D/G-band intensities ($I_{2D}/I_G$) of the graphene film was significantly reduced after transferring to the APS-modified substrate. The blue shift of the 2D position and the reduced $I_{2D}/I_G$ ratio suggested that the graphene layer was effectively doped by the amine functional groups of the APS, consistent with previous reports.[29,30,37]

The effects of the APS doping on the work function of graphene and the electron injection between graphene and PTCDI-C13 were examined by performing UPS analyses of the pristine and APS-doped graphene films. Figure 2a shows the UPS spectra at the secondary electron cutoff region. Here, the work function ($\Phi$) of the graphene films could be derived using the following equation

$$\Phi = h\nu - |E_{sec} - E_{Fermi}|$$

where $h\nu$ = 21.2 eV (He source), $E_{Fermi}$ is the Fermi edge (22.0 eV, obtained from the valence band spectrum under a −5 V applied bias, acquired at the 4D beamline at PAL), and $E_{sec}$ is the onset of secondary emission. The work functions of the

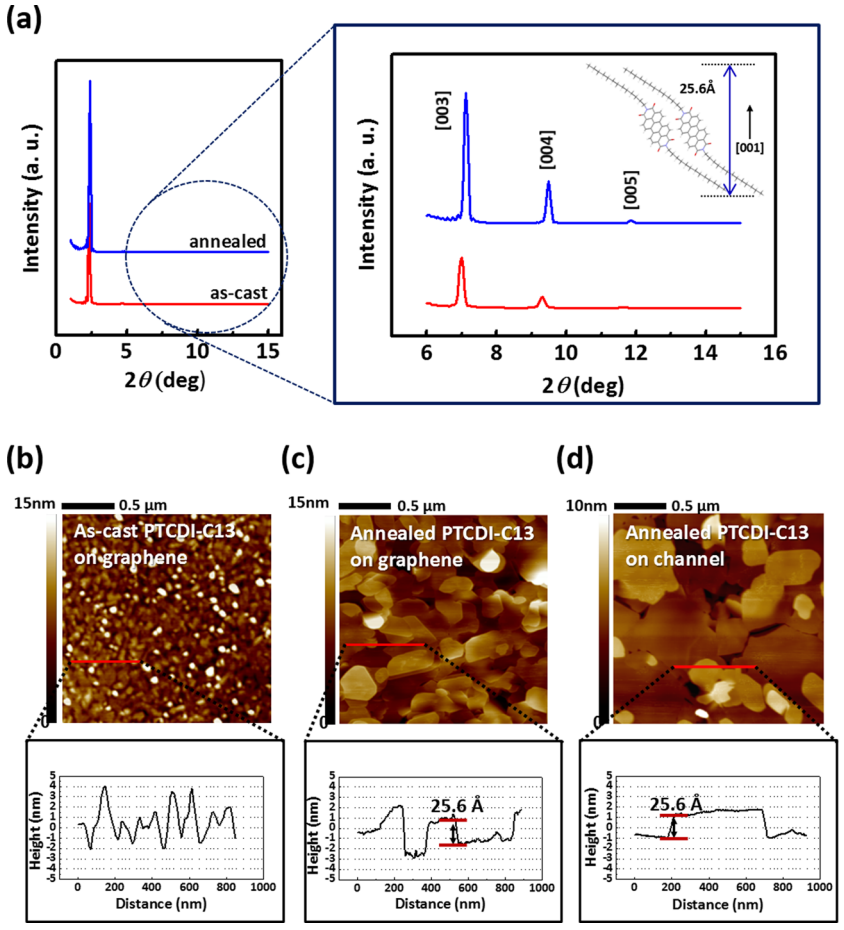


**Figure 3.** (a) $\theta-2\theta$ mode out-of-plane XRD profiles of the as-cast and thermally treated PTCDI-C13 thin films on monolayer graphene ($\lambda$ = 1.07 Å). The inset shows the crystallographic packing pattern of the PTCDI-C13 (CIF file from the reference).[31] AFM topography images of (b) the as-cast PTCDI-C13 film on an n-doped graphene electrode, (c) a thermally-annealed PTCDI-C13 film on an n-doped graphene electrode, and (d) a thermally-annealed PTCDI-C13 film on a channel region. The bottom graphs displayed the corresponding AFM cross-sectional height profiles of the PTCDI-C13 films.

pristine and APS-doped graphene films were calculated to be 4.55 and 3.87 eV, respectively. The reduction in the work function was attributed to the molecular doping by the lone-pair electrons of the amine groups in APS, which increased the Fermi level of graphene from the Dirac point (i.e., introduced *n*-doping).[28,32,33,37] The UPS spectra and reported energy levels of PTCDI-C13[30,38] were used to draw the schematic energy diagrams of the interface between the graphene electrodes and the overlying PTCDI-C13 films.[30,38] As shown in Figure 2b, the calculated electron injection barrier at the interface between the *n*-doped graphene electrode and the PTCDI-C13 was much lower than that at the interface between the pristine graphene electrode and the PTCDI-C13. These results demonstrated that electron injection could be facilitated in OFETs by decreasing the work function of graphene via molecular doping by APS, thereby lowering the injection barrier.

For high OFET performance, it is essential to achieve the high crystalline organic semiconductors characterized by large grains and a molecular assembly structure that favors charge transport in the lateral direction between the S/D electrodes.[2,39] Thermal treatment involving heating at 120°C−140°C induced the formation of large flat grains and enhanced the crystallinity of the PTCDI-C13 on the $SiO_2$ or polymer gate dielectrics, resulting in an optimal OFET performances.[7,31] Accordingly, in this work, we heated the PTCDI-C13 OFETs at 130°C and performed XRD and AFM analyses to examine how the thermal annealing step affected the molecular packing of the PTCDI-C13 on the graphene films. Figure 3a shows the $\theta-2\theta$ mode out-of-plane XRD patterns of PTCDI-C13 films deposited on graphene before and after the thermal treatment. Thermally annealed films showed much higher diffraction peaks compared to the as-deposited films, indicating a higher crystallinity as a result of thermal annealing. The diffraction patterns consisted of [00*l*] peaks with a *d*-spacing of 25.6 Å, obtained from Bragg's law, $2d \sin\theta = n\lambda$. The *d* value corresponded to the c-axis length of the triclinic unit cell of the PTCDI-C13 crystals (25.3 Å),[31] indicating that the PTCDI-C13 molecules were stacked in such a way that the alkyl chains were oriented along surface normal in the out-of-plane direction of the graphene films, as shown schematically in the inset of Figure 3a. This "standing-up" molecular assembly configuration has been shown to be beneficial for OFET operation.[26] Our results contrasted with recent reports on the growth of perylene-3,4,9,10-tetracarboxylic dianhydride (PTCDA) on epitaxially-grown graphene films.[40] PTCDA molecules tend to form well-ordered islands with a herringbone arrangement (i.e., lying-down assembly) on the surfaces of epitaxially grown graphene.[40] The standing-up assembly of PTCDI-C13 molecules in our system may result from the presence of (1) PMMA and photoresist residues on the


dx.doi.org/10.1021/am500618g | ACS Appl. Mater. Interfaces 2014, 6, 6816−6824

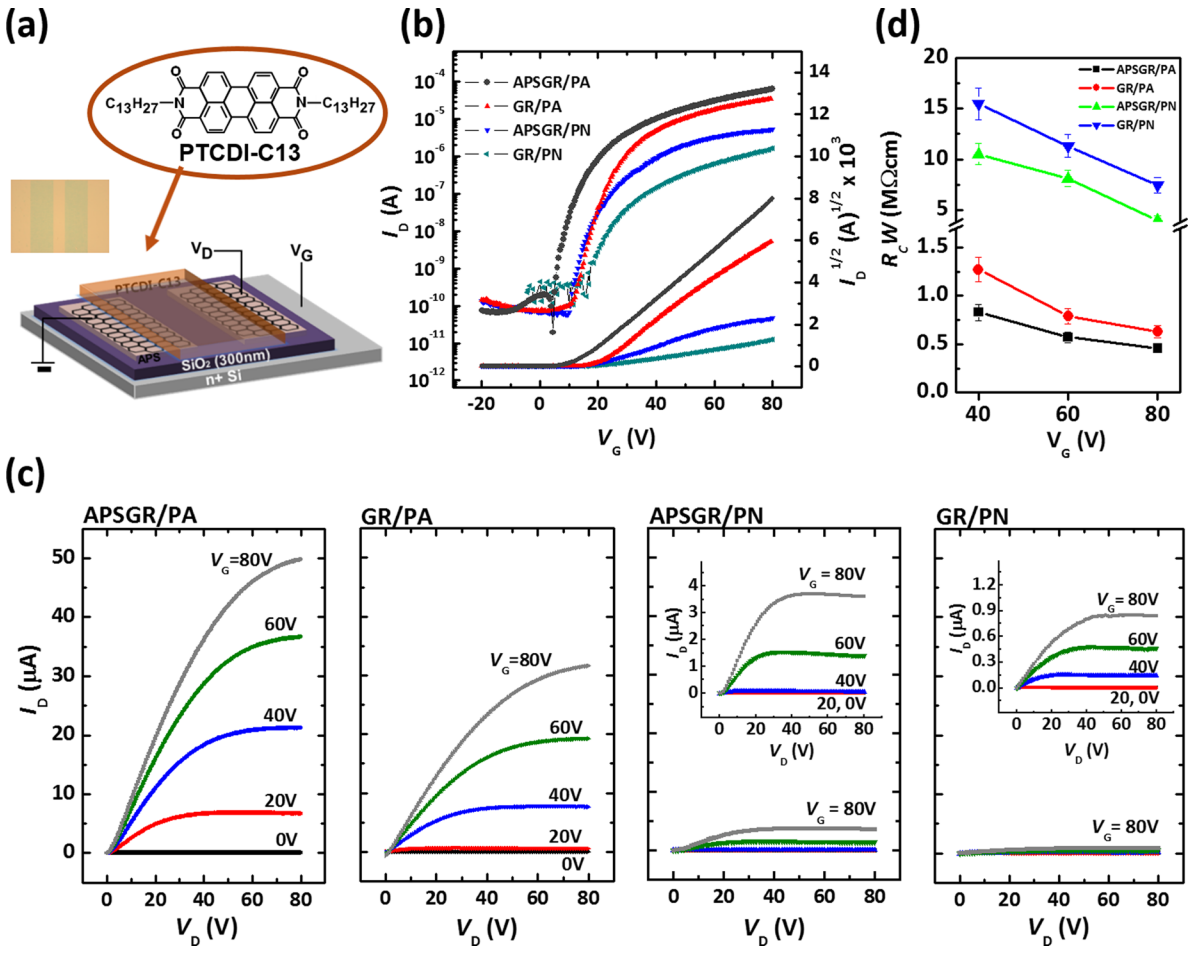


**Figure 4.** (a) Schematic illustration of a bottom-contact PTCDI-C13 OFET prepared using graphene S/D electrodes, used in this study. The left inset shows an optical microscopy image of a patterned graphene electrode, and the right inset shows the chemical structures of N, N′-ditridecyl-3,4,9,10-perylenetetracarboxylic diimide (PTCDI-C13). (b) Transfer in the saturation regime ($V_D$ = 80 V), and (c) output characteristics of the OFETs prepared with the four types of graphene electrodes. The channel lengths ($L$) and widths ($W$) of the OFETs were 100 and 1000 $\mu$m, respectively. The insets in the output characteristics of APSGR/PN and GR/PN show magnified views of the output curves.

surfaces of the CVD-grown graphene after the transfer/patterning processes, and (2) the presence of long alkyl chains in the PTCDI-C13 molecules. In general, polymer residues on the surface of CVD-grown graphene can hinder $\pi-\pi$ interactions between graphene and semiconductor molecules, leading to the standing-up assembly of organic semiconductors.[26] Because PTCDI-C13 molecules have long side chains at the perylene diimide backbone, unlike PTCDA, the long chain can also hinder $\pi-\pi$ interactions between the graphene and perylene diimide backbone.[25] It should be noted that the positions of the PTCDI-C13 film diffraction peaks were shifted slightly toward higher angles after thermal annealing, indicating a slightly reduced $d$-spacing. The shorter interlayer distance in the thermally annealed PTCDI-C13 films, relative to the as-deposited films, suggested that the alkyl side chains in the PTCDI-C13 were interdigitated with other side chains.[41]

Figures 3b, c show AFM topography images and height profiles of the PTCDI-C13 thin films on the graphene S/D electrodes before and after thermal annealing, respectively. The PTCDI-C13 molecules in the as-deposited films on graphene formed ellipsoidal ball-like small grains (Figure 3b), whereas they formed flat sheet-like grains with much larger grain sizes after thermal annealing (Figure 3c). The cross-sectional height profiles of the thermally annealed PTCDI-C13 films revealed that the height of each grain was about 25.6 Å, in good agreement with the XRD analysis. Figure 3d shows the morphology of a PTCDI-C13 film in the channel area between the S/D electrodes of an OFET (i.e., on the $SiO_2$ surface, as shown in Figure 4a) after thermal annealing. The PTCDI-C13 grains in the channel area were slightly larger and flatter than those on the graphene S/D electrodes. The slightly different morphologies of the PTCDI-C13 films over the channel or electrode areas probably resulted from the presence of polymer residues that remained on the graphene surface. These residues possibly disrupted the flat growth of the PTCDI-C13 grains during thermal annealing.[7,25] The XRD and AFM studies suggest that charge transport in OFETs may be facilitated by improving the semiconductor crystallinity, enlarging the grain size via thermal treatment, and inducing favorable molecular assembly of PTCDI-C13 molecules on graphene.

The APS doping of the graphene S/D electrodes and the thermal annealing of the PTCDI-C13 films affected the device characteristics, as determined by measuring the electrical properties of OFETs prepared with the device structure shown in Figure 4a. The effects of doping and thermal annealing were examined by preparing four OFETs prepared under different processing conditions: OFETs prepared using APS-doped graphene electrodes and thermal annealing


dx.doi.org/10.1021/am500618g | ACS Appl. Mater. Interfaces 2014, 6, 6816−6824

**Table I. Electrical Characteristics of the *n*-type PTCDI-C13 OFETs Prepared with Graphene Electrodes**

| device | $\mu_{sat}$ ($cm^2$/(V s)) | $V_{th}$ (V) | $I_{on/off}$ | SS (V/dec) |
|---|---|---|---|---|
| APSGR/PA | 0.40 ± 0.03 | 8.84 ± 0.93 | ~1 × $10^6$ | −3.45 ± 0.13 |
| GR/PA | 0.22 ± 0.03 | 17.93 ± 1.49 | ~1 × $10^5$ | −3.88 ± 0.11 |
| APSGR/PN | 0.11 ± 0.04 | 17.28 ± 1.71 | ~1 × $10^5$ | −3.28 ± 0.15 |
| GR/PN | 0.01 ± 0.005 | 23.40 ± 4.52 | ~1 × $10^5$ | −5.07 ± 0.21 |

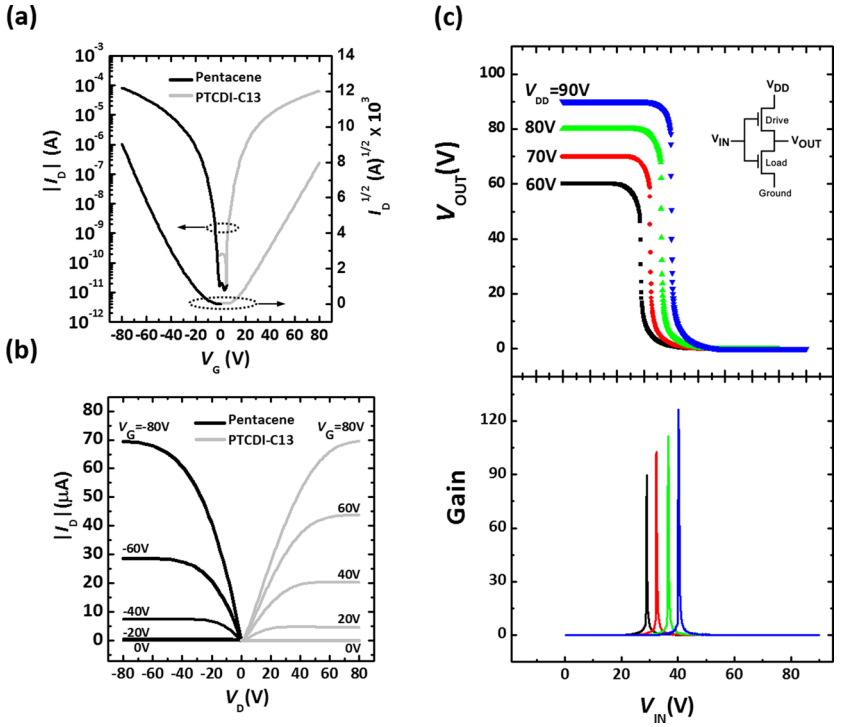


**Figure 5.** (a) Transfer in the saturation regime, and (b) output characteristics of the pentacene and PTCDI-C13 OFETs. The channel lengths ($L$) and widths ($W$) of the OFETs were 100 and 1000 $\mu$m, respectively. (c) The voltage transfer characteristics (top) and DC voltage gain (bottom) of the inverter with various $V_{DD}$ values. The inset shows a schematic diagram of the inverter structure based on the zero drive load logic: with the load transistor and the drive transistor ($W/L$= 1600 $\mu$m/150 $\mu$m).

(denoted as APSGR/PA), OFETs prepared using pristine graphene electrodes and thermal annealing (denoted as GR/PA), OFETs prepared using APS-doped graphene and without annealing (denoted as APSGR/PN), and OFETs prepared using pristine graphene electrodes without annealing (denoted as GR/PN). Panels b and c in Figure 4, respectively, show the transfer and output characteristics of these OFETs. The field-effect mobility ($\mu$) was calculated in the saturation regime (drain voltage, $V_D$ = 80 V) from the slope of the square root drain current ($I_D^{1/2}$) versus the gate voltage ($V_G$) using the equation, $I_D = \mu C_i W(2L)^{-1}(V_G - V_{th})^2$, where $C_i$ is the capacitance per unit area of the gate dielectrics (10 nF/$cm^2$) and $V_{th}$ is the threshold voltage. All electrical characteristics of these OFETs are summarized in Table I. Compared to the OFETs prepared without annealing (APSGR/PN and GR/PN), the thermally annealed OFETs (APSGR/PA and GR/PA) showed higher mobilities and on-state currents. These results demonstrated that a higher PTCDI-C13 crystallinity and grain size as a result of thermal annealing improved the OFET performance. In addition, the OFETs prepared using APS-doped graphene S/D electrodes (APSGR/PA or APSGR/PN) exhibited better performances than their pristine graphene electrode counterparts (GR/PA or GR/PN), confirming that a lower injection barrier between the graphene and PTCDI-C13 layers benefitted the device operation. Among these OFETs, the APSGR/PA devices yielded the highest transistor performance, with an average $\mu$ value of 0.40 ± 0.03 $cm^2$/Vs obtained from 12 different devices prepared under each condition. This $\mu$ value is higher than that of any other reported *n*-type bottom-contact OFETs prepared with metal, conducting polymer, or other nanomaterial S/D electrodes.[16,42−44] We also fabricated *n*-type OFETs made of aluminum S/D electrodes, but these OFETs showed very poor performance ($\mu \leq 0.001$ $cm^2$/(V s) ) with severe electrical noises in the saturation region, as shown in Figure S4 in the Supporting Information. The reason why the APSGR/PA devices had higher $\mu$ value than that of *n*-type bottom-contact OFETs made of other electrode materials is that (1) CVD-grown graphene had lower surface roughness and better thermal stability than other electrode materials,[22−26] thereby facilitating to optimize the molecular ordering and grain growth of the PTCDI-C13, and (2) the low work function metals are readily oxidized and formed a thin metal oxide layer that significantly impeded the charge injection into the PTCDI-C13, whereas CVD-grown graphene did not form oxide layer over its surface.[16,18,19]

It should be noted that the APSGR/PA devices also showed the smallest contact resistance between the graphene S/D electrode and the active layer. The width-normalized contact resistances ($R_cW$) of the OFETs under various gate voltages are summarized in Figure 4d. In general, a low injection barrier, a

high crystallinity, and large grain sizes in the organic semiconductor layers over the S/D electrodes led to smaller values of $R_cW$, which enhanced the OFET performance.[16−18,25−27] In APSGR/PA, the lower injection barrier at the interface between APS-doped graphene S/D electrodes and PTCDI-C13, the higher crystallinity, and larger grain size of thermally annealed PTCDI-C13 collectively contributed to lowered contact resistance.[43] Moreover, because thermal annealing also increased the crystallinity and grain size of the PTCDI-C13 layer over the channel area, it can facilitate lateral charge transport in the channel region, and therefore can reduce the channel resistance.[7,31] Therefore, we believe that the reduced contact and channel resistances both appeared to contribute to the high OFET performance of the APSGR/PA devices.

The performances of APSGR/PA devices approached the performances obtained from *p*-type pentacene OFETs using graphene S/D electrodes, as shown in panels a and b in Figure 5. AFM topography images in Figure S5 showed that many grains of pentacene were grown on the graphene electrodes, and the resulting OFETs exhibited a field-effect mobility of 0.44 ± 0.02 $cm^2/Vs$, which was comparable to the state-of-the-art value reported for pentacene OFETs prepared using CVD-grown and photo-lithography-patterned graphene S/D electrodes.[27,28] For the pentacene OFETs, graphene S/D electrodes did not need to be *n*-doped because it is unnecessary to reduce the work function of graphene. Actually, the pentacene OFETs prepared using APS-doped graphene S/D electrodes exhibited lower transfer performances with $\mu$ value of 0.15 $cm^2/(V\ s)$ than their pristine graphene electrode, shown in Figure S6 in the Supporting Information. Organic complementary inverters were constructed as described Figure S2 in the Supporting Information. The APS SAM was patterned on the substrate by exposing the surface to UV-ozone through a shadow mask prior to graphene transfer, to obtain *p*-type pentacene OFETs. The APS SAM was effectively removed under UV-ozone exposure, as confirmed by the contact angle and XPS measurements, as shown in Figure S7 in the Supporting Information. The organic inverters showed good voltage transfer characteristics (VTCs) over a range of operating voltages, from 60 to 90 V, as shown in Figure 5c. The output voltage ($V_{OUT}$) was almost the same as the supply voltage ($V_{DD}$) when the input voltage ($V_{IN}$) was lower than the switching threshold voltage ($V_M$). For $V_{IN}$ is exceeding $V_M$, the *p*- and *n*-type OFETs, respectively, turned off and on, leading to an almost zero $V_{OUT}$. The $V_M$ were found to be 28.9, 32.4, 36.6, and 40.3 V for $V_{DD}$ values of 60, 70, 80, and 90 V, respectively, corresponding closely to half of the supply voltage $V_{DD}$. These results suggested that our inverters could operate with very good noise margins for potential applications in integrated circuits. The noise margin values were roughly estimated by calculating the voltage at $(dV_{OUT}/dV_{IN}) = -1$, the forbidden region.[45,46] The low and high noise margins were found to be 36.2 and 44.9 V, respectively, for $V_{DD}$ of 90 V. These values were more than 80% of the theoretical values (i.e., 0.5 × $V_{DD}$).[45,46] Another important figure-of-merit of the inverters is the inverter voltage gain, defined as $dV_{OUT}/dV_{IN}$. The average voltage gain of the maximum values extracted from VTCs with $V_{DD}$ values of 60, 70, 80, and 90 V was well above 100. The highest gain was obtained from the VTC with a $V_{DD}$ of 90 V: 124. To the best of our knowledge, this voltage gain is among the highest values yet reported for inverters based on bottom-contact OFET structures.[44,47−49] The good noise margins and high voltage gains of the inverters were attributed to the balanced performances of the *n*- and *p*-type OFETs, which resulted in reasonably high field-effect mobility values.

## CONCLUSIONS

In conclusion, we demonstrated the preparation of high-performance organic complementary inverters using monolayer graphene S/D electrodes consisting of *n*-type PTCDI-C13 OFETs and *p*-type pentacene OFETs. The work function of the graphene electrodes used to prepare the *n*-type OFETs was lowered by the presence of an underlying APS SAM, which introduced molecular doping to the graphene surface and reduced the electron injection barrier between the graphene and the PTCDI-C13. Thermal annealing the PTCDI-C13 OFETs remarkably improved the crystallinity and facilitated the growth of PTCDI-C13 grains on the graphene electrode surfaces. The thermally annealed *n*-type OFETs prepared using APS-doped graphene electrodes exhibited superior field-effect mobility values up to 0.43 $cm^2/(V\ s)$, with high on/off ratios exceeding $1 \times 10^6$. These values were comparable to those of the *p*-type pentacene OFETs. Good agreement between the electrical properties of the *p*- and *n*-type OFETs resulted in an outstanding inverter gain, in excess of 124, and good noise margins during the highly symmetric operation of the complementary inverters. This study will contribute to the realization of organic integrated devices based on CVD-grown graphene electrodes.

## ASSOCIATED CONTENT

### Supporting Information

Optical microscopy image of patterned graphene electrodes for OFETs, and magnified optical images, optical microscopy image of patterned graphene electrodes for inverters, schematic diagram of the fabrication steps used to prepare the organic complementary inverters with selectively patterned APS-doped graphene electrodes, width-normalized total resistance ($R_{total}W$) values for the APSGR/PA and GR/PA devices, transfer characteristics in the saturation regime ($V_D$ = −80 V) of the PTCDI-C13 OFETs based on aluminum S/D electrodes, AFM topography image of the pentacene film on graphene electrode without APS SAM, transfer characteristics in the saturation regime ($V_D$ = −80 V) of the pentacene OFETs based on graphene S/D electrodes with/without (black circle) APS treatment, and XPS profiles and contact angles of the pristine $SiO_2$/Si and surface-modified $SiO_2$/Si substrates before and after UV exposure. This material is available free of charge via the Internet at http://pubs.acs.org.

## AUTHOR INFORMATION

### Corresponding Author

*E-mail: cep@postech.ac.kr. Fax: +82-54-279-8298. Tel: +82-54-279-2269.

### Notes

The authors declare no competing financial interest.

## ACKNOWLEDGMENTS

The authors thank Dr. Won Min Yun for experimental support and helpful discussions. This work was supported by a grant (2011-0031639) from the Center for Advanced Soft Electronics under the Global Frontier Research Program of the Ministry of Education, Science and Technology, Korea. The authors also thank the Pohang Accelerator Laboratory for providing access to the 4D and the 5A beamlines used in this study.

## REFERENCES


(1) Sirringhaus, H.; Brown, P. J.; Friend, R. H.; Nielsen, M. M.; Bechgaard, K.; Langeveld-Voss, B. M. W.; Spiering, A. J. H.; Janssen, R. A. J.; Meijer, E. W.; Herwig, P.; De Leeuw, D. M. Two-Dimensional Charge Transport in Self-Organized, High-Mobility Conjugated Polymers. *Nature* **1999**, *401*, 685−688.

(2) Klauk, H. Organic Thin-Film Transistors. *Chem. Soc. Rev.* **2010**, *39*, 2643−2666.

(3) Sekitani, T.; Zschieschang, U.; Klauk, H.; Someya, T. Flexible Organic Transistors and Circuits with Extreme Bending Stability. *Nat. Mater.* **2010**, *9*, 1015−1022.

(4) Huang, T.-H.; Lai, H.-C.; Tzeng, B.-J.; Pei, Z. Air Stable Organic Complementary Inverter with High and Balance Noise Margin Based on Polymer/metal Oxide Hybrid Gate Dielectrics. *Org. Electron.* **2012**, *13*, 1365−1369.

(5) Zhao, Y.; Di, C.-a; Gao, X.; Hu, Y.; Guo, Y.; Zhang, L.; Liu, Y.; Wang, J.; Hu, W.; Zhu, D. All-Solution-Processed, High-Performance n-Channel Organic Transistors and Circuits: Toward Low-Cost Ambient Electronics. *Adv. Mater.* **2011**, *23*, 2448−2453.

(6) Baeg, K.-J.; Khim, D.; Jung, S.-W.; Kang, M.; You, I.-K.; Kim, D.-Y.; Facchetti, A.; Noh, Y.-Y. Remarkable Enhancement of Hole Transport in Top-Gated N-Type Polymer Field-Effect Transistors by a High-k Dielectric for Ambipolar Electronic Circuits. *Adv. Mater.* **2012**, *24*, 5433−5439.

(7) Jang, J.; Nam, S.; Chung, D. S.; Kim, S. H.; Yun, W. M.; Park, C. E. High Tg Cyclic Olefin Copolymer Gate Dielectrics for N,N′-Ditridecyl Perylene Diimide Based Field-Effect Transistors: Improving Performance and Stability with Thermal Treatment. *Adv. Funct. Mater.* **2010**, *20*, 2611−2618.

(8) Yan, H.; Chen, Z.; Zheng, Y.; Newman, C.; Quinn, J. R.; Dötz, F.; Kastler, M.; Facchetti, A. A High-Mobility Electron-Transporting Polymer for Printed Transistors. *Nature* **2009**, *457*, 679−686.

(9) Letizia, J. A.; Salata, M. R.; Tribout, C. M.; Facchetti, A.; Ratner, M. A.; Marks, T. J. n-Channel Polymers by Design: Optimizing the Interplay of Solubilizing Substituents, Crystal Packing, and Field-Effect Transistor Characteristics in Polymeric Bithiophene-Imide Semiconductors. *J. Am. Chem. Soc.* **2008**, *130*, 9679−9694.

(10) Yun, S. W.; Kim, J. H.; Shin, S.; Yang, H.; An, B.-K.; Yang, L.; Park, S. Y. High-Performance n-Type Organic Semiconductors: Incorporating Specific Electron-Withdrawing Motifs to Achieve Tight Molecular Stacking and Optimized Energy Levels. *Adv. Mater.* **2012**, *24*, 911−915.

(11) Lv, A.; Puniredd, S. R.; Zhang, J.; Li, Z.; Zhu, H.; Jiang, W.; Dong, H.; He, Y.; Jiang, L.; Li, Y.; Pisula, W.; Meng, Q.; Hu, W.; Wang, Z. High Mobility, Air Stable, Organic Single Crystal Transistors of an n-Type Diperylene Bisimide. *Adv. Mater.* **2012**, *24*, 2626−2630.

(12) Chua, L.-L.; Zaumseil, J.; Chang, J.-F.; Ou, E. C.-W.; Ho, P. K.-H.; Sirringhaus, H.; Friend, R. H. General Observation of n-Type Field-Effect Behaviour in Organic Semiconductors. *Nature* **2005**, *434*, 194−199.

(13) Kim, S. H.; Jang, M.; Yang, H.; Anthony, J. E.; Park, C. E. Physicochemically Stable Polymer-Coupled Oxide Dielectrics for Multipurpose Organic Electronic Applications. *Adv. Funct. Mater.* **2011**, *21*, 2198−2207.

(14) Jang, J.; Nam, S.; Yun, W. M.; Yang, C.; Hwang, J.; An, T. K.; Chung, D. S.; Park, C. E. High Tg Cyclic Olefin copolymer/Al2O3 Bilayer Gate Dielectrics for Flexible Organic Complementary Circuits with Low-Voltage and Air-Stable Operation. *J. Mater. Chem.* **2011**, *21*, 12542.

(15) Lu, Y.; Lee, W. H.; Lee, H. S.; Jang, Y.; Cho, K. Low-Voltage Organic Transistors with Titanium Oxide/polystyrene Bilayer Dielectrics. *Appl. Phys. Lett.* **2009**, *94*, 113303.

(16) Hong, K.; Kim, S. H.; Yang, C.; An, T. K.; Cha, H.; Park, C.; Park, C. E. Photopatternable, Highly Conductive and Low Work Function Polymer Electrodes for High-Performance n-Type Bottom Contact Organic Transistors. *Org. Electron.* **2011**, *12*, 516−519.

(17) Yun, D.-J.; Kim, J.-M.; Ra, H.; Byun, S.; Kim, H.; Park, G.-S.; Park, S.; Rhee, S.-W. The Physical/chemical Properties and Electrode Performance Variations of SWNT Films in Consequence of Solution Based Surfactant Elimination Processes. *Org. Electron.* **2013**, *14*, 2962−2972.

(18) Zhou, Y.; Fuentes-Hernandez, C.; Shim, J.; Meyer, J.; Giordano, A. J.; Li, H.; Winget, P.; Papadopoulos, T.; Cheun, H.; Kim, J.; Fenoll, M.; Dindar, A.; Haske, W.; Najafabadi, E.; Khan, T. M.; Sojoudi, H.; Barlow, S.; Graham, S.; Bredas, J.-L.; Marder, S. R.; Kahn, A.; Kippelen, B. A Universal Method to Produce Low-Work Function Electrodes for Organic Electronics. *Science* **2012**, *336*, 327−332.

(19) Hirose, Y.; Kahn, A.; Aristov, V.; Soukiassian, P.; Bulovic, V.; Forrest, S. Chemistry and Electronic Properties of Metal-Organic Semiconductor Interfaces: Al, Ti, In, Sn, Ag, and Au on PTCDA. *Phys. Rev. B* **1996**, *54*, 13748−13758.

(20) Geim, A. K.; Novoselov, K. S. The Rise of Graphene. *Nat. Mater.* **2007**, *6*, 183−191.

(21) Schedin, F.; Geim, A. K.; Morozov, S. V.; Hill, E. W.; Blake, P.; Katsnelson, M. I.; Novoselov, K. S. Detection of Individual Gas Molecules Adsorbed on Graphene. *Nat. Mater.* **2007**, *6*, 652−655.

(22) Li, X.; Cai, W.; An, J.; Kim, S.; Nah, J.; Yang, D.; Piner, R.; Velamakanni, A.; Jung, I.; Tutuc, E.; Banerjee, S. K.; Colombo, L.; Ruoff, R. S. Large-Area Synthesis of High-Quality and Uniform Graphene Films on Copper Foils. *Science* **2009**, *324*, 1312−1314.

(23) Kim, K. S.; Zhao, Y.; Jang, H.; Lee, S. Y.; Kim, J. M.; Kim, K. S.; Ahn, J.-H.; Kim, P.; Choi, J.-Y.; Hong, B. H. Large-Scale Pattern Growth of Graphene Films for Stretchable Transparent Electrodes. *Nature* **2009**, *457*, 706−710.

(24) Bae, S.; Kim, H.; Lee, Y.; Xu, X.; Park, J.-S.; Zheng, Y.; Balakrishnan, J.; Lei, T.; Kim, H. R.; Il Song, Y.; Kim, Y.-J.; Kim, K. S.; Ozyilmaz, B.; Ahn, J.-H.; Hong, B. H.; Iijima, S. Roll-to-Roll Production of 30-Inch Graphene Films for Transparent Electrodes. *Nat. Nanotechnol.* **2010**, *5*, 574−578.

(25) Jang, J.; Park, J.-S.; Nam, S.; Anthony, J. E.; Kim, Y.; Kim, K. S.; Kim, K. S.; Hong, B. H.; Park, C. E. Self-Organizing Properties of Triethylsilylethynyl-Anthradithiophene on Monolayer Graphene Electrodes in Solution-Processed Transistors. *Nanoscale* **2013**, *5*, 11094−11101.

(26) Lee, W. H.; Park, J.; Sim, S. H.; Lim, S.; Kim, K. S.; Hong, B. H.; Cho, K. Surface-Directed Molecular Assembly of Pentacene on Monolayer Graphene for High-Performance Organic Transistors. *J. Am. Chem. Soc.* **2011**, *133*, 4447−4454.

(27) Lee, S.; Jo, G.; Kang, S.-J.; Wang, G.; Choe, M.; Park, W.; Kim, D.-Y.; Kahng, Y. H.; Lee, T. Enhanced Charge Injection in Pentacene Field-Effect Transistors with Graphene Electrodes. *Adv. Mater.* **2011**, *23*, 100−105.

(28) Lee, W. H.; Park, J.; Kim, Y.; Kim, K. S.; Hong, B. H.; Cho, K. Control of Graphene Field-Effect Transistors by Interfacial Hydrophobic Self-Assembled Monolayers. *Adv. Mater.* **2011**, *23*, 3460−3464.

(29) Yan, Z.; Sun, Z.; Lu, W.; Yao, J.; Zhu, Y.; Tour, J. M. Controlled Modulation of Electronic Properties of Graphene by Self-Assembled Monolayers on $SiO_2$ Substrates. *ACS Nano* **2011**, *5*, 1535−1540.

(30) Park, J.; Lee, W. H.; Huh, S.; Sim, S. H.; Kim, S. B.; Cho, K.; Hong, B. H.; Kim, K. S. Work-Function Engineering of Graphene Electrodes by Self-Assembled Monolayers for High-Performance Organic Field-Effect Transistors. *J. Phys. Chem. Lett.* **2011**, *2*, 841−845.

(31) Tatemichi, S.; Ichikawa, M.; Koyama, T.; Taniguchi, Y. High Mobility n-Type Thin-Film Transistors Based on N, N′-Ditridecyl Perylene Diimide with Thermal Treatments. *Appl. Phys. Lett.* **2006**, *89*, 112108.

(32) Sojoudi, H.; Baltazar, J.; Tolbert, L. M.; Henderson, C. L.; Graham, S. Creating Graphene p-n Junctions Using Self-Assembled Monolayers. *ACS Appl. Mater. Interfaces* **2012**, *4*, 4781−4786.

(33) Jang, Y.; Cho, J. H.; Kim, D. H.; Park, Y. D.; Hwang, M.; Cho, K. Effects of the Permanent Dipoles of Self-Assembled Monolayer-Treated Insulator Surfaces on the Field-Effect Mobility of a Pentacene Thin-Film Transistor. *Appl. Phys. Lett.* **2007**, *90*, 132104.

(34) Lee, W. H.; Park, J.; Sim, S. H.; Jo, S. B.; Kim, K. S.; Hong, B. H.; Cho, K. Transparent Flexible Organic Transistors Based on Monolayer Graphene Electrodes on Plastic. *Adv. Mater.* **2011**, *23*, 1752−1756.

(35) Zeng, X.; Xu, G.; Gao, Y.; An, Y. Surface Wettability of (3-Aminopropyl)triethoxysilane Self-Assembled Monolayers. *J. Phys. Chem. B* **2011**, *115*, 450−454.
(36) Morrill, A. R.; Duong, D. T.; Lee, S. J.; Moskovits, M. Imaging 3-Aminopropyltriethoxysilane Self-Assembled Monolayers on Nanostructured Titania and Tin (IV) Oxide Nanowires Using Colloidal Silver Nanoparticles. *Chem. Phys. Lett.* **2009**, *473*, 116−119.
(37) Dong, X.; Fu, D.; Fang, W.; Shi, Y.; Chen, P.; Li, L.-J. Doping Single-Layer Graphene with Aromatic Molecules. *Small* **2009**, *5*, 1422−1426.
(38) Wan, A. S.; Long, J. P.; Kushto, G.; Mäkinen, A. J. The Interfacial Chemistry and Energy Level Structure of a Liquid Crystalline Perylene Derivative on Au(111) and Graphite Surfaces. *Chem. Phys. Lett.* **2008**, *463*, 72−77.
(39) Jang, J.; Nam, S.; Im, K.; Hur, J.; Cha, S. N.; Kim, J.; Son, H. B.; Suh, H.; Loth, M. A.; Anthony, J. E.; Park, J.-J.; Park, C. E.; Kim, J. M.; Kim, K. Highly Crystalline Soluble Acene Crystal Arrays for Organic Transistors: Mechanism of Crystal Growth During Dip-Coating. *Adv. Funct. Mater.* **2012**, *22*, 1005−1014.
(40) Wang, Q. H.; Hersam, M. C. Room-Temperature Molecular-Resolution Characterization of Self-Assembled Organic Monolayers on Epitaxial Graphene. *Nat. Chem.* **2009**, *1*, 206−211.
(41) An, T. K.; Kang, I.; Yun, H.-J.; Cha, H.; Hwang, J.; Park, S.; Kim, J.; Kim, Y. J.; Chung, D. S.; Kwon, S.-K.; Kim, Y. H.; Park, C. E. Solvent Additive to Achieve Highly Ordered Nanostructural Semicrystalline DPP Copolymers: Toward a High Charge Carrier Mobility. *Adv. Mater.* **2013**, *25*, 7003−7009.
(42) Lee, J. S.; Kim, N. H.; Kang, M. S.; Yu, H.; Lee, D. R.; Oh, J. H.; Chang, S. T.; Cho, J. H. Wafer-Scale Patterning of Reduced Graphene Oxide Electrodes by Transfer-and-Reverse Stamping for High Performance OFETs. *Small* **2013**, *9*, 2817−2825.
(43) Hong, K.; Kim, S. H.; Yang, C.; Jang, J.; Cha, H.; Park, C. E. Improved n-Type Bottom-Contact Organic Transistors by Introducing a Poly(3,4-Ethylenedioxythiophene):poly(4-Styrene Sulfonate) Coating on the Source/drain Electrodes. *Appl. Phys. Lett.* **2010**, *97*, 103304.
(44) Yun, D.-J.; Hong, K.; Kim, S. H.; Yun, W.-M.; Jang, J.; Kwon, W.-S.; Park, C.-E.; Rhee, S.-W. Multiwall Carbon Nanotube and Poly(3,4-Ethylenedioxythiophene): Polystyrene Sulfonate (PEDOT:PSS) Composite Films for Transistor and Inverter Devices. *ACS Appl. Mater. Interfaces* **2011**, *3*, 43−49.
(45) Rabaey, J. M. *Digital Integrated Circuits: A Design Perspective*, 1st ed.; Prentice Hall: Upper Saddle River, NJ, 1995.
(46) Zhang, X.-H.; Potscavage, W. J.; Choi, S.; Kippelen, B. Low-Voltage Flexible Organic Complementary Inverters with High Noise Margin and High Dc Gain. *Appl. Phys. Lett.* **2009**, *94*, 043312.
(47) Briseno, A. L.; Tseng, R. J.; Li, S.-H.; Chu, C.-W.; Yang, Y.; Falcao, E. H. L.; Wudl, F.; Ling, M.-M.; Chen, H. Z.; Bao, Z.; Meng, H.; Kloc, C. Organic Single-Crystal Complementary Inverter. *Appl. Phys. Lett.* **2006**, *89*, 222111.
(48) Min, S.-Y.; Kim, T.-S.; Kim, B. J.; Cho, H.; Noh, Y.-Y.; Yang, H.; Cho, J. H.; Lee, T.-W. Large-Scale Organic Nanowire Lithography and Electronics. *Nat. Commun.* **2013**, *4*, 1773.
(49) Khim, D.; Baeg, K.-J.; Kim, J.; Yeo, J.-S.; Kang, M.; Amegadzea, P. S. K.; Kim, M.-G.; Cho, J.; Lee, J. H.; Kim, D.-Y.; Noh, Y.-Y. Electron Injection Enhancement by a Cs-Salt Interlayer in Ambipolar Organic Field-Effect Transistors and Complementary Circuits. *J. Mater. Chem.* **2012**, *22*, 16979.